

CHAPTER XXX

IMAGING OF NANOSCALE PHOTOGENERATED CHARGE TRANSPORT IN ORGANIC PHOTOVOLTAIC MATERIALS

Behrang Hamadani^a, Paul M. Haney^b and Nikolai B. Zhitenev^b

^a*Engineering Laboratory, ^bCenter for Nanoscale Science and Technology
National Institute of Standards and Technology
20899, Gaithersburg, MD, USA
E-mail: zhitenev@nist.gov*

Photogenerated charge transport in bulk heterojunction (BHJ) solar cells is strongly dependent on the active layer nanomorphology. Local probes have been extensively employed to understand the correlation between 2D and 3D morphology and device efficiency, with varying degree of success. Here, we address some outstanding metrological challenges using a set of complementary measurement approaches and theoretical modeling. Specifically, we study nanoscale morphological and functional properties of BHJ using (1) nanopatterned metal contacts (2) direct electrical probes using tips with different work functions, which collect either electrons or holes at the top surface in different device stacks (3) wedge-shaped devices to investigate vertical material phase segregation.

1. Introduction

Bulk heterojunction (BHJ) organic solar cells have shown significant improvement in performance over the last few years^{1,2} and much effort is under way to further elucidate the photophysical phenomena and the mechanisms responsible for charge generation and transport in these systems.^{3,4} Charge transport in blended organic BHJ on solar cells is strongly influenced by the nanoscale morphology and materials self-organization of the donor and acceptor networks.⁵⁻¹⁰ The morphology is often crucially dependent on the processing conditions such as the heat

and solvent annealing, and the improvement in device performance is generally associated with optimal phase segregation, both for the in-plane and vertical directions¹¹⁻¹³, a higher degree of crystallinity, and enhanced charge carrier mobility.⁵⁻⁸

A variety of scanning probe techniques and microscopies have been employed to investigate the role of nanomorphology on charge transport in organic photovoltaic (OPV) films. More insight is frequently obtained when structural characterizations are combined with optical or electrical measurements at the nanoscale. Conductive-tip atomic force microscopy (AFM) has been performed to investigate dark conductivities and local current-voltage variations in blended OPV films.¹⁴⁻¹⁶ Other scanning probe techniques employed to date include photoconductive AFM to study photocurrent variations due to film nanomorphology,¹⁷⁻¹⁹ scanning Kelvin probe microscopy (SKPM) for studying the surface potential,²⁰⁻²² near-field scanning optical microscopy (NSOM) to investigate local photoluminescence or photocurrent,^{22,23} and scanning transmission x-ray microscopy for studying of nanoscale chemical composition in these films.²⁴

While the application of these various scanning probe microscopy (SPM) techniques for characterization of OPV materials has been very enlightening, many metrological issues need to be resolved to infer a quantitative information relevant to device performance. The following topics require further consideration and elaboration, and will be addressed in this chapter:

(1) The physics and chemistry of contacts and contact interfaces are absolutely essential for device operation. Contacts with different work functions break the inversion symmetry of the effectively isotropic bulk material providing the electric field which drives electrons and holes in opposite directions for extraction to the external circuit. The fact that the contact interfaces are an integral part of the device makes it extremely challenging to determine parameters relevant for device operation from SPM experiments. If SPM characterization is performed without contacts at the material surface (e.g. SKPM or surface photovoltage microscopy), it is unclear how such measurements can be ultimately related to device characteristics. On the other hand, in contact mode SPM experiments, the interface between scanning probe and OPV material is

very different in structure and composition from that in devices, and the relevance of the measurement has to be further investigated.

(2) SPM measurements are mainly suited for two-dimensional (2-D) characterization, while OPV device operation is dependent on its three-dimensional (3-D) material morphology. The overall 3-D morphology is caused by material self-organization and can be subtly dependent on details of the materials processing and the substrate. While some assumption about material distribution as a function of depth can be made based on advanced modes of SPM, in general, full 3-D morphology cannot be extracted from 2-D measurements. The unknown 3-D material organization can lead to significant ambiguity in interpretation of some SPM measurements, e.g. contact AFM.

(3) The geometry and boundary conditions of contact AFM or STM measurements are different from the large planar contact geometry typical for devices. The current or photocurrent spreading in “point” measurements, spatial distribution of voltage around the contact point on the top surface, possible presence of traps at the exposed top surface, and additional surface recombination can all significantly affect the local measurements complicating direct comparison with properties of large devices.

In the following, we will discuss some experimental and modeling approaches aimed to clarify these measurement problems.

2. Local photocurrent measured with nano-contacts of different size.

The first set of measurement problems outlined above motivated us to fabricate nano-contacts for use as local probes of photo-current in OPV materials. To reproduce the composition and structure of the large device contact, we fabricate small contacts with a similar process, rather than relying on the bare scanning tip-OPV interface contact. Modern lithography techniques should enable, in principle, fabrication of contacts with sizes comparable to the resolution of SPM experiments. In addition, the size of fabricated contacts can be conveniently scaled up to experimentally clarify the issues related to the geometry of the

measurements (issue (3) described in the Introduction). Here, local photocurrent measurements based on a polymer/fullerene OPV blend will be discussed.

Blended poly(3-hexylthiophene) and phenyl-C61-butyric acid methyl ester (P3HT:PCBM, 1:1) films were prepared by spin-coating followed by solvent and heat annealing of the film on Poly(3,4-ethylenedioxythiophene) poly(styrenesulfonate) (PEDOT:PSS) coated indium tin oxide (ITO) electrodes. We employed a fabrication recipe known to produce highest efficiency devices.²⁵ The active layer film thickness was typically around 140 nm as verified by spectroscopic ellipsometry and profilometry. Devices with mm-sized top and bottom electrodes (top electrode: Ca/Ag (thickness 40/100 nm respectively)) were fabricated and measured separately on similarly prepared films, showing excellent I-V characteristics (FF=60 %, $J_{SC}=11 \text{ mA cm}^{-2}$, $V_{OC}=0.6 \text{ V}$, where FF is the fill factor, J_{SC} is the short circuit current density and V_{OC} is the open circuit voltage). Typical devices showed power conversion efficiency (PCE) of $3.9 \% \pm 0.4 \%$ without correction for the calibration mismatch factor, estimated to lower the PCE by a factor of ≈ 0.7 .²⁰

Standard electron-beam lithography techniques could not be used to pattern metal directly on top of organic film. Instead, the nanoscale contacts were deposited by metal evaporation through silicon nitride stencil masks with arrays of small openings in the shape of dots as defined by e-beam lithography and an etch process.²⁶ The nanodot arrays were designed with different diameters with the smallest nanodots on the OPV film formed with 300 nm diameter openings. We note that the nucleation and growth of metals on organic films is generally dependent on a variety of factors,²⁷ such as the sticking coefficient and the evaporation rate, and this may be further complicated by the constricted geometry of the masks. We avoided using Au, Pt or other high work function materials because their use as cathode electrodes in devices results in poor open circuit voltage and low photogenerated current. We chose Ag over other lower work function metals such Al or Ca because it oxidizes at a much slower pace and the reproducibility of the nanodevices was better. The AFM tip used for probing the nanodots is a boron-doped conductive diamond-coated tip. All measurements were

performed in a dry, N_2 environment. The AFM chamber was equipped with an optical fiber illuminating the sample from the bottom, and estimated laser power levels at the sample were $\approx 2\text{W cm}^{-2}$ at the laser wavelength of 532 nm. AFM was also used for topographic measurements and for direct photo-current measurements as will be discussed below.

The measured surface topography by itself is very rough with peak to valley variations of up to 40 % of the total film thickness. This roughness is the result of the low spin rate from a hot solvent and the slow drying of the film under the solvent anneal process.¹ In Fig. 1, we show the photocurrent response of the nanodots under short circuit conditions with the photocurrent color-coded map superimposed directly on top of the 3-D topography data. Among different dots, a significant variation (up to a factor of 10) in photocurrent response is observed. We do not find any consistent correlation between the topography and the photocurrent data suggesting that the variations in the material organization that gives rise to the topographical features have only minor effects on device performance. The variations in the nanodot photoresponse is not related to the tip/nanodot contact quality as repeated scans over the same area and other arrays of nanodots produce identical results. Current-voltage characteristics from several of these dots in the dark are shown in the inset of Fig. 1b. Most show relatively well-behaved diode-like response with low reverse saturation currents and high forward bias currents (substrate bias with respect to the tip). The main panel of Fig. 1b shows the I-V characteristics under illumination. With the bias voltage applied to the ITO film and the polarity of the V_{OC} as obtained (positive V_{OC} and photocurrent crossing from negative to positive), the electrons are collected from the top while holes reach the ITO, similar in behavior to large-scale devices. Since electrons are accepted and transported via PCBM networks, the data suggest that the nanodots with the greatest response are in intimate contact with PCBM regions near the surface.

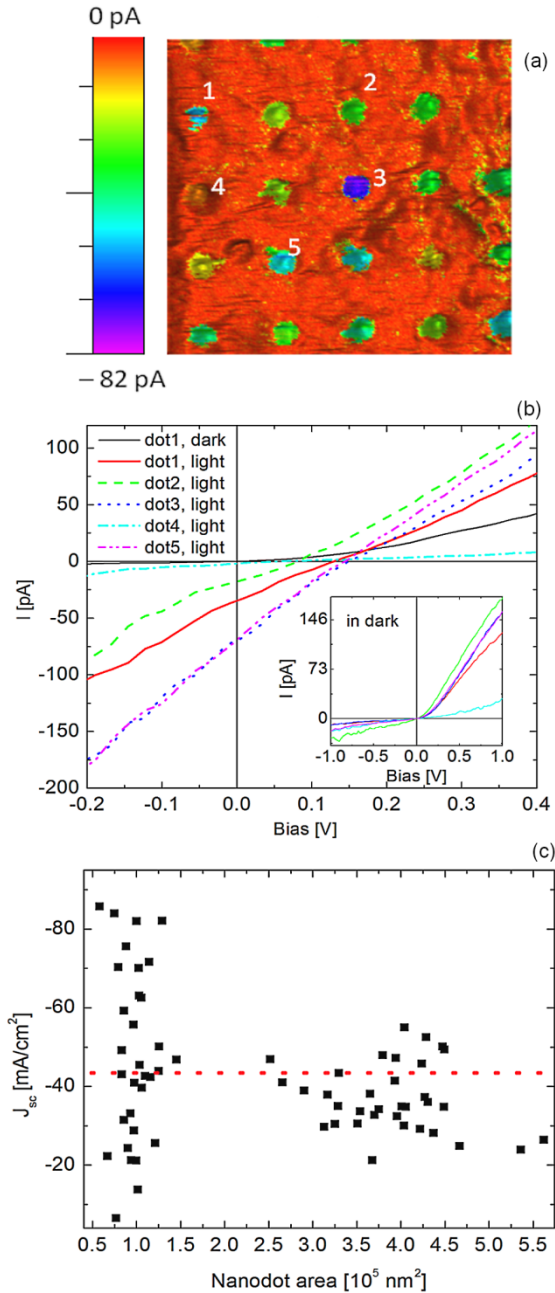


Fig. 1 (a) Photoresponse of a 300 nm nanodot array under short circuit illumination conditions with the photocurrent color-coded map superimposed directly on top of the surface representation of topography data. The scan area is 4500 nm by 4500 nm. (b) (Inset) Dark I-V characteristics of 5 arbitrary nanodots as marked on the graph. (Main) I-V characteristics of the same devices under illumination. (c) Short circuit current density as a function of the nanodot area for a variety of nanocontacts, showing large fluctuations for smaller dots.

The nanodots exhibit a nearly linear photoresponse in reverse bias (FF of $\approx 25\%$). While this has been associated with recombination losses due to low dissociation efficiency of bound electron-hole pairs in other OPV systems,^{28,29} we attribute it to the high illumination intensities necessary to observe robust (pA) currents on the nanoscale and the role of the ever-present finite series resistance. In order to perform a careful study of this phenomenon, we independently measured the I-V characteristics of a mm-sized device with a Ca/Ag cathode as a function of light intensity (with a solar simulator).²⁵ As the light intensity increases, the FF is reduced and the reverse bias dependence of the current becomes more significant. At intensities of about 1 W cm^{-2} (10 suns) and higher, the I-V curves look approximately linear with FF reduced to 25% (from 70% at low intensities), all very consistent with the nanodot I-V characteristics at the laser illumination intensities of the experiment ($\approx 2\text{ W cm}^{-2}$ (20 suns)).

A detailed analysis of nanodot photoresponse vs. size shows that as the nanodots size increases, the fluctuations in the short circuit current density among different dots are reduced. This can be seen clearly in Fig. 1c, where the J_{SC} from several scans over variety of arrays is plotted as a function of the nanodot area. For small size nanodot arrays, the fluctuations can be as large as a factor of 10, while fluctuations are reduced as the dot sizes grow, indicating an averaging that takes place over areas of high and low current. We find an average current density of $\approx 43\text{ mA cm}^{-2}$ under our illumination conditions ($\approx 2\text{ W cm}^{-2}$ or 20 suns) for all types of dot arrays (with diameters ranging from 300 nm to 600 nm). These numbers are consistent with large contact device parameters at high light intensity.³⁰

From this experiment we see that the measured current approaches large contact value when the contact size is a few times larger than the film thickness. For smaller contacts, the large current variation can be caused by other inhomogeneity at small scales. Below, we will further investigate the origin of this inhomogeneity.

We note that some important device parameters, most notably V_{OC} values measured in large devices, could not be reproduced in this experiment. One possible reason is that the contact work function, chemistry and morphology are still quite different than those in large

devices. For example, we could not introduce Ca underlayer into our nano-contact stack as such contacts always appear insulating in the measurement, likely because of exposed edges and accelerated oxidation. In large Ag devices, similarly low V_{OC} has been attributed to oxidation of the cathode³¹.

3. Surface and bulk characterization: morphology and photo-current

To further address the issue of significant photo-current variation on small length scales, we have performed direct photocurrent measurements with the AFM tip (PCAFM). The diamond-coated tips used for transport measurements from the nanodots work very well for direct contact and photocurrent measurements from the bare OPV film yield V_{OC} values similar to those observed with nano-contacts. We also experimented with tips made from different materials, and some results will be discussed in the next section. We attribute the good PCAFM images to the relatively low work function (4.1 ± 0.5 eV grown on (111)-oriented substrates)³² of the boron-doped diamond tips resulting in better band alignment for electron photocurrent collection from the PCBM regions (with lowest unoccupied molecular orbital (LUMO) position estimated at ≈ 4.0 eV).³¹

Figure 2a shows a 3-D plot of the film topography overlaid with the photocurrent map collected simultaneously with a conductive diamond-coated AFM tip under illumination at short circuit conditions. Consistent with the previous observations on the nanodots, we do not observe any specific correlation between topography and photoconductive response, i.e., areas of low or high current are observed throughout the film without a clear topographical correlation. It is noted however that since the tip radius of curvature is very large (≈ 100 nm), topographical features appear smooth in the scans, but photocurrent features as small as 50 nm can be detected. The variations in photocurrent are large and can be as high as an order of magnitude of change over lateral dimensions as small of as 100 nm. In this regard, the largest photocurrent is observed in small regions which we refer to as “hot spots” of current on the order of tens of nm, occasionally growing in size up to 200 nm. In between the

hot-spot regions (green and blue) there are regions of intermediate conductance (yellow color) that can extend larger in size, but the majority of film surface is relatively non-photoconductive (red). A flooding analysis of this image reveals that the total area of the photocurrent response above the floor noise (yellow through violet) only constitutes (20 to 30) % of the total area of the film. Open circuit

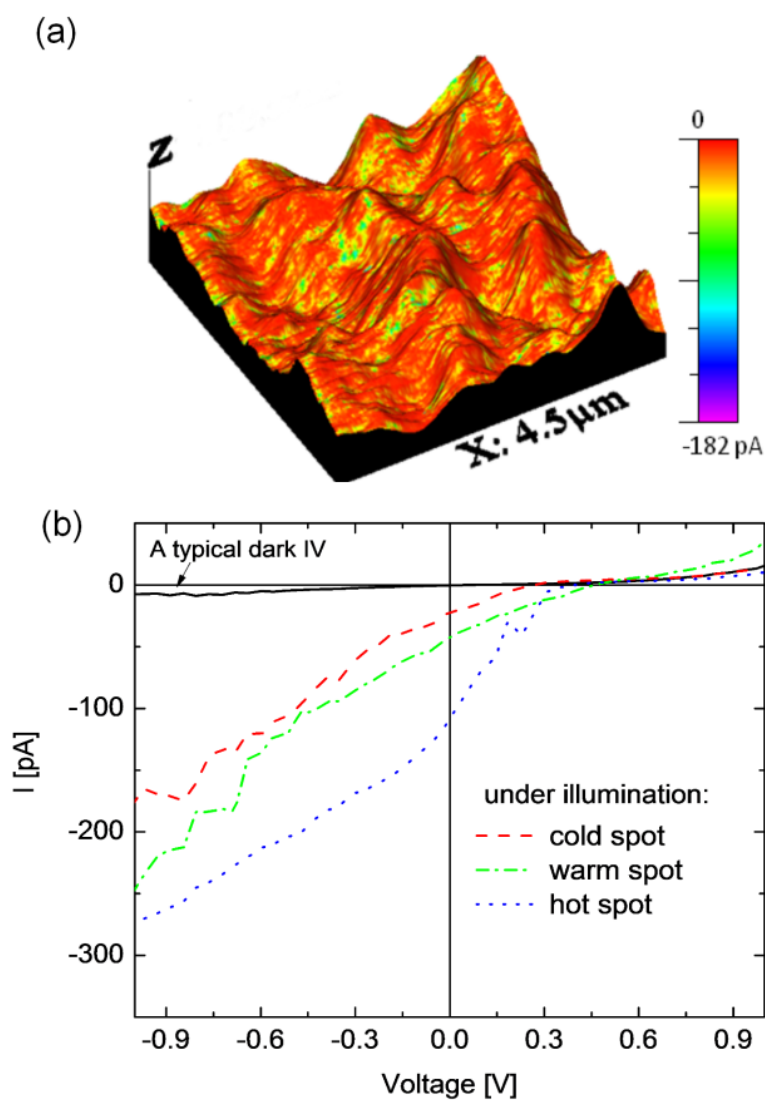


Fig.2: (a) Surface plot of the film topography overlaid with the photocurrent map collected simultaneously with a conductive diamond-coated AFM tip under short circuit conditions. Topography scale (Z) is 100 nm. (b) Local I-V measurements on 3 representative spots across the film surface: a cold spot (orange to yellow colors), a warm spot (green color), and a hot spot (blue or purple).

voltages in the range of 0.3 V to 0.45 V measured in the hot-spots are very similar to those observed in macroscopic devices fabricated with Al top contacts³¹, further validating that the diamond tip work function is similar to Al. From the polarity of V_{OC} and the sign of I , we observe that the photogenerated holes are collected from the ITO contact and electrons, transported via the PCBM networks, are collected at the top surface with the AFM tip; therefore, the hot spots are expected to originate from transport of electrons by PCBM regions to the tip. Our results suggest that only about 25 % of the air-exposed surface of the OPV film is enriched with PCBM. Statistical analysis of the data of Fig. 2 by construction of an “imaginary” nanodot array on that surface based on integrating the local photocurrent response over regions of fixed area leads to photoresponse variations very similar to those shown in Fig. 1a with “real” contacts.

The PCAFM results from the top surface are consistent with an electron blocking skin layer (P3HT) with lateral scale of hundreds of nm and dilute hot spots corresponding to PCBM nanocrystals on or near the top surface. The current does not appear to directly reflect the bulk morphology, which recent TEM tomography studies have revealed to exhibit much finer structures and a more uniform blending.^{9,10} This surface composition therefore does not represent the true nanoscale bulk morphology of this system: The surface phase segregation is on the order of hundreds of nanometers, whereas the exciton diffusion length in these organic systems is much smaller, on the order of 20 nm or less²²; in contrast, the length scale of phase segregation in the bulk must be similar to the exciton diffusion length to explain observed quantum efficiencies as high as 60 %² and a well-quenched photoluminescence spectrum.²³ In an attempt to access the bulk nanomorphology, we have used ultralow angle microtomy to make cuts in the OPV film, removing the surface layer and creating exposed wedges along the cut directions.²⁵

Figure 3a shows high-resolution intermittent contact AFM images of the top of the film with a Si_3N_4 tip with 10 nm radius of curvature; this data is consistent with AFM scans of similarly prepared films in the literature. Figure 3b shows a scan from the wedge region with much finer morphology. These images clearly show that the air-exposed morphology does not represent the material blending in the bulk, but is

enriched with a P3HT skin layer. This has been independently demonstrated by XPS and NEXAFS measurements.¹³ From several line scans along the transition region from the bulk to the top surface morphology, we estimate that the top layer thickness is ≈ 10 nm or less.

Figures 3c and 3d show PCAFM data from the top and the bulk region, respectively demonstrating that without the top skin layer, the bulk photoresponse is much more uniform across the film, although the low resolution of the diamond tip (100 nm radius of curvature) does not

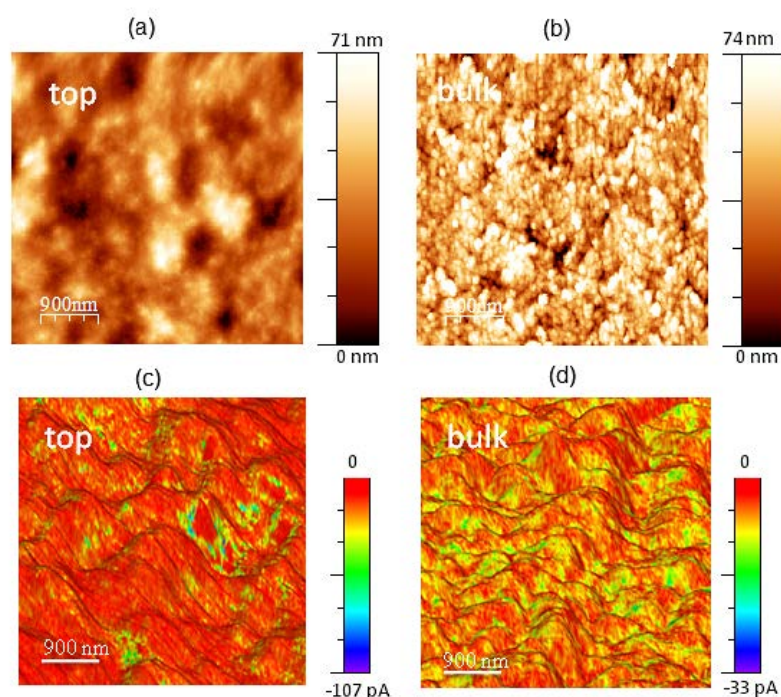


Fig. 3: High-resolution intermittent-contact AFM images of the top OPV film (a) and the bulk film (b) after being exposed by cutting a wedge in the film with a low angle microtome technique (c,d) Color-coded photocurrent data superimposed on 3D rendering of the topography scans for the top and bulk of the film respectively. Bulk photoresponse is measured under a small substrate bias of -0.3 V for improved signal-to-noise.

allow us consistently correlate the photoresponse with the material phases in observed in Fig. 3b. This confirms that the skin layer is directly

responsible for low photocurrent yield from large areas of the top surface.

Since most of the top surface represents a very inefficient contact for electron extraction, we need to understand how this affects the device properties. The high external quantum efficiency (peaking around 60 %) and conversion efficiency of these cells suggest that the hot spots in the surface are adequate to harvest the majority of the bulk carriers. It is surprising that the vertical phase segregation which leads to mostly polymer (hole-transporting) interface near the electron collector does not significantly degrade efficiency.

To understand this further, we theoretically studied the effect of a nonuniform donor (D)-acceptor (A) blend on organic photovoltaic (OPV) device performance³³. We employed a one-dimensional model including a drift-diffusion equation to describe electron and hole transport, a field and temperature dependent generation and recombination rate that captures the exciton physics, and the Poisson equation for electrostatics. To this model we added the effect of a spatially varying effective density of states (EDOS) that describes the number of D and A states per volume. We found that the main effect of a nonuniform D-A blend is on the charge generation and resulting short-circuit current: in regions where the blend is primarily of one type at the expense of the other, there is less charge generation due to a reduced D-A interfacial area. The influence of a nonuniform blend on electron and hole transport is a weaker effect. Fig. 4a illustrates this with a series of hypothetical D-A blends. Fig. 4b shows results for a D-A blend with a skin layer of one type- as found experimentally. It is found that the change in efficiency is small (a maximum of 10% change) as the skin layer goes from mostly D-like to an even D-A mix to mostly A-like (the experimentally realistic case is a mostly D-like skin layer). The intuitive picture that emerges from this analysis is that electrons and holes can very easily “squeeze” through regions of reduced density.

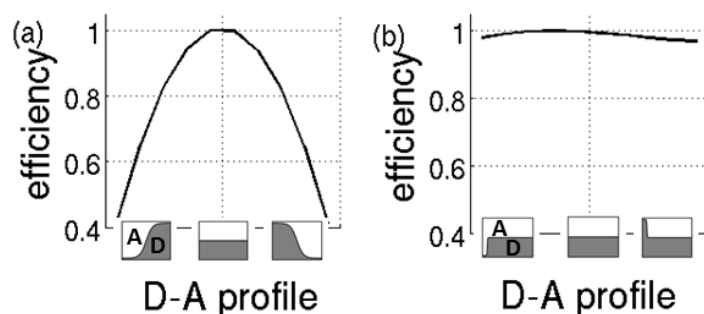


Fig. 4. Efficiency evolution as the spatial distribution of donor (D) and acceptor (A) molecules is continuously varied (the cartoons along the x-axis illustrates the spatial profiles). (a) uses a hypothetical spatial distribution that varies widely throughout the layer. (b) shows the experimentally relevant skin layer; the skin layer is localized near the left-hand contact, and varies from mostly A to mostly D.

The main limitation of this model is its restriction to 1-d. When the EDOS is small, the charge and current density are also small. However, experiments reveal localized hot-spots of conducting paths. A 1-d model necessarily averages these localized hot-spots or large current density over the entire cross-sectional area, leading to a diffuse current. As the overall area of hot-spots decreases, the charge and current density they must accommodate increases and the current may become space-charge limited. A 1-d model is unable to capture the physics described in this scenario. However, for less extreme cases, the treatment described here offers the simplest account for a spatially varying blend structure.

4. Tip work function and pc-AFM of normal and inverted OPV structures

In a general case, the photoconductive AFM under bias measures both the collection of the photogenerated carriers and the charge injection into donor and acceptor networks. To understand local current-voltage characteristics, both processes have to be properly accounted for. Both processes can be sensitively dependent on the tip work function relative to the local work function of OPV blend. Further exploiting our knowledge of the vertical phase segregation and the top surface nanomorphology of P3HT:PCBM devices,²⁵ we analyze the details of PCAFM contrast at the sample surface.³⁴ In addition to “normal” devices studied above, we fabricate “inverted” devices where *holes* are collected

at the top surface. We study local photocurrent on both normal and inverted devices using AFM tips with work a suitable function for the collection of the appropriate charge (i.e., electrons vs. holes). We then explore the role of the film/tip contact on the local current-voltage (I-V) characteristics of these structures and analyze physical models capable of reproducing the qualitative features of the data.

Normal device structures were prepared as described above. For inverted devices, a solution of titanium isopropoxide, prepared by a previously published method,³⁵ was spun cast on ITO-coated glass at 2000 2π rad/min for 60 s, followed by a high temperature anneal at 400 °C on a hot plate for 1 h to remove organic residue and improve electrical performance of the film. The OPV layer was then spun-cast onto TiO₂ coated ITO in the exact manner described above. For complete device testing, 40 nm of Ca followed by 100 nm of Ag was thermally evaporated onto OPV films for normal devices, and 40 nm of Au was thermally deposited onto OPV layer for inverted devices. The device structures are illustrated in Fig. 5a.

The PCAFM measurements performed on the OPV film under illumination at the short circuit conditions in the normal and inverted geometry are shown in Fig. 5b and 5c, respectively, measured with different AFM tips. For these figures, we have overlaid the photocurrent response onto the 3D topography of the active layer, where the red color represents little or no current and green and blue colors represent high photocurrent response. The measurements reveal extreme heterogeneity of the photoresponse. In Fig. 5b, the PCAFM map measured with a moderate work function conductive diamond coated (CDC) tip shows local hot spots of photoresponse corresponding to photogenerated electron current from PCBM regions at the top surface,²⁵ while the majority of the surface area displays very low current as described in the previous section.

In the inverted geometry, holes are collected at the top surface and, since the surface is mostly enriched by P3HT, the majority of the surface should show high photoresponse, but of the opposite current sign. This is confirmed by the map in Fig. 5c, where we employed a high work function Pt coated AFM tip to collect the hole current from the surface. The percentage of the area displaying high positive photocurrent in

inverted device ($\approx 80\%$) is very similar to the area of low current in the normal device in Fig. 5b. The complementary character of these maps

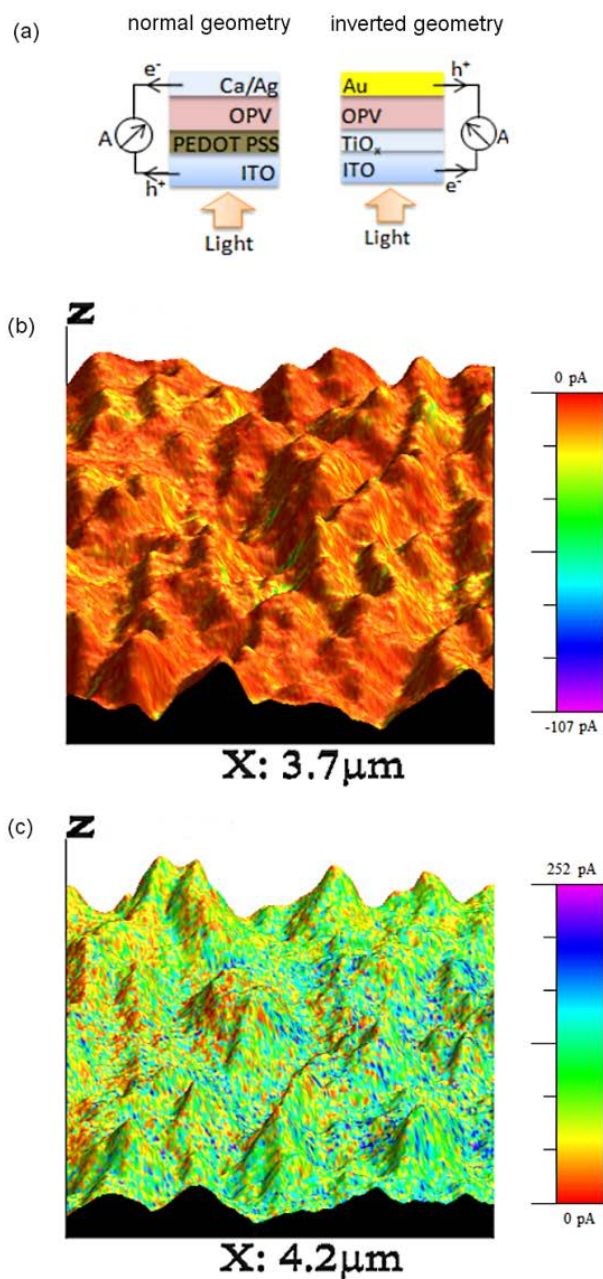


Fig. 5 (a) Schematics for the normal and inverted device geometries. (b) 3D plot of the film topography overlaid with the photocurrent map collected simultaneously under short circuit illumination conditions for the normal device geometry with a conductive diamond coated AFM tip. Z scale is 37 nm (c) A similar figure for the inverted geometry with a Pt coated AFM tip. The bias voltage is applied to the ITO electrode with respect to the tip in both cases. Z scale is 64 nm

proves that (1) the material composition at the top interface for both device geometries consists mostly of polymer and (2) under short-circuit condition and suitable tip work functions, PCAFM yield reliable information on materials composition.

However, the local I-V curves (Fig. 6a-b) look qualitatively different from those observed in macroscopic devices with nearly ideal diode-like characteristics. Figure 6a shows the I-V data measured by the CDC tip on the film in the normal geometry, with negative voltage corresponding to the reverse bias. In the dark, the typical I-V data at all locations on the film surface show a leaky diode-like behavior. Under illumination, the sign of I_{SC} and V_{OC} corresponds to electron collection from the tip under

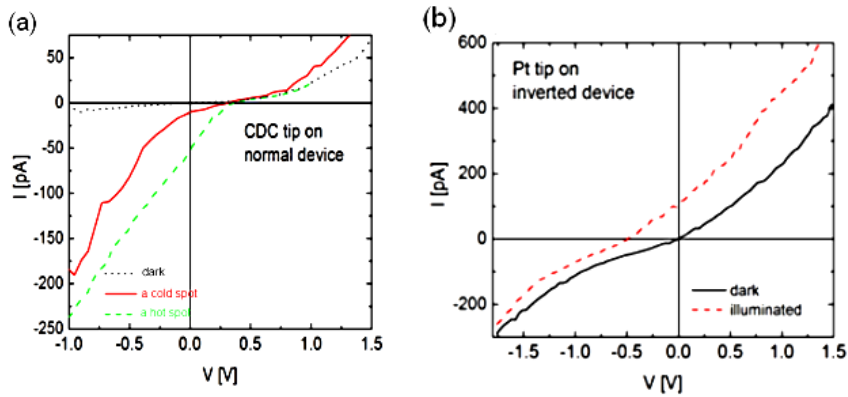


Fig.6. (a) Local dark and light IV measurements with the conductive diamond coated tip on the normal device structure in the dark and at two spots (b) Local dark and light I-V measurements with the Pt tip on the inverted device structure.

short circuit conditions. Although the FF is low ($\approx 12\%$), V_{OC} range from 0.3 V to 0.4 V, similar to devices with Ag or Al contacts.³¹ At mediocre (low photocurrent or cold spots) spots, the I-V response shows a nonlinear increase of current with voltage under the reverse bias, or counter-diode behavior. At very bright hot spots, the FF is larger ($\approx 25\%$), and the current increases linearly under the reverse bias or, in some cases, shows signs of saturation. In the forward bias, I-V curves in both light and dark are similar and appear to be limited by the series resistance.

For inverted devices (Figs. 6b), we observe hole collection from the tip under the short circuit conditions (opposite sign of voltage and current) both with both the CDC (not shown) and the Pt tips. However, the Pt tip shows higher photocurrent and improved FF in the second quadrant compared to the CDC data, indicating that Pt coated tips are better suited for hole collection. This is likely due to a better band alignment between the highest occupied molecular orbital (HOMO) of P3HT (≈ 5.1 eV) and Fermi level of Pt metal. For both data sets, the dark I-Vs show significant leakage and counter-diode response in the reverse bias (positive voltages).

We are interested in identifying possible physical mechanisms that lead to the highly non-ideal I-V characteristics measured with the conductive AFM. In particular, we would like a quantitative model that reproduces the reverse bias turn-on under illumination seen in the point contact in the normal device geometry. A 1-d model which leads to this qualitative behavior is described in our previous publication.³⁵ Briefly, it consists of a Schottky contact at the AFM-OPV interface, where we postulate localized states very near the contact which become occupied upon illumination. This leads to an electrostatic field which reduces the barrier for charge injection, facilitating reverse bias current flow. It is difficult, however, to fit the experimental data with this model, using realistic parameters. This suggests that other factors, such as the nontrivial 3-d geometry of the system, may be at play. In particular, the electrostatic field responsible for charge collection is localized near the tip-surface interface. Its spatial extent (and therefore the region of charge collection, and ensuing photocurrent), is dependent on the applied bias, and on the system dimensionality. A reverse bias voltage increases the spatial extent of the field, increasing the photocurrent, and providing some non-trivial dependence of the current on the reverse bias. This effect can not be adequately captured in a 1-d model. Another important consideration is the non-ideality of the AFM-OPV interface. This may be described by a low surface recombination velocity S_R . Sufficiently small values of S_R can lead to non-ideal, "S-shaped" I-V curves.³⁷

5. Conclusions

We have demonstrated that a number of challenges in determining local composition and functionality of OPV devices described in the Introduction can be successfully addressed using a set of complementary measurements and modeling approaches. In particular, we have demonstrated that:

(1) measurements using nanocontacts can provide current-voltage characteristics similar to large devices, although it is rather challenging to achieve high VOC. Photocurrent is largely confined to contacts area for contact sizes $\approx 1 \mu\text{m}$ or above, and current spreading beyond the immediate contact area is not too significant. For smaller scales, photocurrent strongly fluctuates due to material segregation at the top surface.

(2) Three-dimensional morphology can be accessed using proper cross-sectioning techniques in combination with photocurrent and non-contact AFM imaging

(3) With the proper choice of scanning tip material, photocurrent maps under short-circuit condition reliably represent the material segregation at the top surface.

Understanding local (photo)current-voltage characteristics in a satisfactory manner and relating these to large device performance still remains an outstanding problem. The characteristics are significantly different from the macroscopic measurements, and can be affected by multiple parameters discussed in introduction and throughout the text that are specific to local measurements. We evaluated possible contribution of some parameters using simplified theoretical models. Qualitative features of I-V characteristics can be described theoretically by a number of different mechanisms, although determining the relative importance of different contributions is still an outstanding problem. More experimental and theoretical work is needed to quantitatively relate local measurements to large-area device performance. Nevertheless the approaches described here illustrate that qualitative conclusions that are relevant for device performance can be made, and point the way to progress towards quantitative understanding.

Acknowledgments

We gratefully acknowledge significant contribution and useful discussion with Lee Richter, Suyong Jung, Nadine Gergel-Hackett, A. Alec Talin, Amit Agrawal, Henri Lezec, Dean DeLongchamp, and David Gundlach. This work has been made possible with the nanofabrication tools and staff support of the NIST Center for Nanoscale Science and Technology.

References

1. G. Li, V. Shrotriya, J. Huang, Y. Yao, T. Moriarty, K. Emery, and Y. Yang, *Nature Mater.* **4**, 864 (2005).
2. J. Peet, J. Y. Kim, N. F. Coates, W. L. Ma, D. Moses, A. J. Heeger, and G. C. Bazan, *Nature Mater.* **6**, 497 (2007).
3. H. Ohkita, S. Cook, Y. Astuti, W. Duffy, S. Tierney, W. Zhang, M. Heeney, I. McCulloch, J. Nelson, D. D. C. Bradley, and J. R. Durrant, *J. Am. Chem. Soc.* **130**, 3030 (2008).
4. C. Urich, D. Wynands, S. Olthof, M. K. Riede, K. Leo, S. Sonntag, B. Maennig, and M. Pfeiffer, *J. Appl. Phys.* **104**, 043107 (2008).
5. G. Li, Y. Yao, H. Yang, V. Shrotriya, G. Yang, and Y. Yang, *Adv. Funct. Mater.* **17**, 1636 (2007).
6. G. Li, V. Shrotriya, J. Huang, Y. Yao, T. Moriarty, K. Emery, and Y. Yang, *Nature Mater.* **4**, 864 (2005).
7. W. Ma, C. Yang, X. Gong, K. Lee, and A. J. Heeger, *Adv. Funct. Mater.* **15**, 1617 (2005).
8. X. Yang, J. Loos, S. C. Veenstra, W. J. H. Verhees, M. M. Wienk, J. M. Kroon, M. A. J. Michels, and R. A. J. Janssen, *Nano. Lett.* **5**, 579 (2005).
9. S. S. van Bavel, E. Sourty, G. de With, and J. Loos, *Nano. Lett.* **9**, 507 (2009).
10. S. S. van Bavel, E. Sourty, G. de With, K. Frolic, and J. Loos, *Macromolecules* **42**, 7396 (2009).
11. M. Campoy-Quiles, T. Ferenczi, T. Agostinelli, P. G. Etchegoin, Y. Kim, T. D. Anthopoulos, P. N. Stavrinou, D. D. C. Bradley, and J. Nelson, *Nature Mater.* **7**, 158 (2008).
12. Z. Xu, L.-M. Chen, G. Yang, C.-H. Huang, J. Hou, Y. Wu, G. Li, C.-S. Hsu, and Y. Yang, *Adv. Funct. Mater.* **19**, 1 (2009).
13. D. S. Germack, C. K. Chan, B. H. Hamadani, L. J. Richter, D. A. Fischer, D. J. Gundlach, and D. M. DeLongchamp, *Appl. Phys. Lett.* **94**, 233303 (2009).
14. O. Douhéret, L. Lutsen, A. Swinnen, M. Bresselge, K. Vandewal, L. Goris, and J. Manca, *Appl. Phys. Lett.* **89**, 032107 (2006).
15. A. Alexeev, J. Loos, and M. M. Koetse, *Ultramicroscopy* **106**, 191 (2006).
16. M. Dante, J. Peet, and T.-Q. Nguyen, *J. Phys. Chem.* **C112**, 7241 (2008).

17. D. C. Coffey, O. G. Reid, D. B. Rodovsky, G. P. Bartholomew, and D. S. Ginger, *Nano Lett.* **7**, 738 (2007).
18. L. S. C. Pingree, O. G. Reid, and D. S. Ginger, *Nano Lett.* **9**, 2946 (2009).
19. M. Chiesa, L. Bürgi, J.-S. Kim, R. Shikler, R. H. Friend, and H. Sirringhaus, *Nano Lett.* **5**, 559 (2005).
20. K. Maturova, M. Kemerink, M. M. Wienk, D. S. H. Charrier, and R. A. J. Janssen, *Adv. Funct. Mater.* **19**, 1379 (2009).
21. A. Liscio, G. De Luca, F. Nolde, V. Palermo, K. Mullen, and P. Samori, *J. Am. Chem. Soc.* **130**, 780 (2008).
22. J. Chappell, D. G. Lidzey, P. C. Jukes, A. M. Higgins, R. L. Thompson, S. O'Connor, I. Grizzi, R. Fletcher, J. O'Brien, M. Geoghegan, and R. A. L. Jones, *Nature Mater.* **2**, 616 (2003).
23. R. Riehn, R. Stevenson, D. Richards, D.-J. Kang, M. Blamire, A. Downes, and F. Cacialli, *Adv. Funct. Mater.* **16**, 469 (2006).
24. C. R. McNeill, B. Watts, L. Thomsen, W. J. Belcher, N. C. Greenham, and P. C. Dastoor, *Nano Lett.* **6**, 1202 (2006).
25. B. H. Hamadani, S. Jung, P. M. Haney, L. J. Richter, and N. B. Zhitenev, *Nano Lett.* **10**, 1611 (2010).
26. M. M. Deshmukh, D. C. Ralph, M. Thomas, and J. Silcox, *Appl. Phys. Lett.* **75**, 1631 (1999).
27. V. Zaporozhchenko, T. Strunskus, K. Behnke, C. V. Bechtolshim, A. Thran, and F. Faupel, *Microelec. Eng.* **50**, 465 (2000).
28. M. M. Mandoc, W. Veurman, L. J. A. Koster, B. de Boer, and P. W. M. Blom, *Adv. Funct. Mater.* **17**, 2167 (2007).
29. S. M. Sze, *Semiconductor Devices* (Wiley, New York, 1985).
30. B. J. Leever, M. F. Durstock, M. D. Irwin, A. W. Hains, T. J. Marks, L. S. C. Pingree, and M. C. Hersam, *Appl. Phys. Lett.* **92**, 013302 (2008).
31. M. O. Reese, M. S. White, G. Rumbles, D. S. Ginley, and S. E. Shaheen, *Appl. Phys. Lett.* **92**, 053307 (2008).
32. M. W. Geis, J. A. Gregory, and B. B. Pate, *IEEE. Trans. Electron Devices* **38**, 619 (1991).
33. P. M. Haney, *J. Appl. Phys.* **110**, 024305 (2011).
34. N. Gergel-Hackett, B. H. Hamadani, B. Dunlap, J. Suehle, C. Richter, C. Hacker, and D. Gundlach, *IEEE. Elect. Dev. Lett.* **30**, 706 (2009).
35. B. H. Hamadani, N. Gergel-Hackett, P. M. Haney, and N. B. Zhitenev, *J. Appl. Phys.* **109**, 124501 (2011).
36. L. J. A. Koster, E. C. P. Smits, V. D. Mihailetschi, and P. W. M. Blom, *Phys. Rev.* **B72**, 085205 (2005).
37. A. Wagenpfahl, D. Rauh, M. Binder, C. Deibel, and V. Dyakonov, *Phys. Rev.* **B82**, 115306 (2010).